AIMS Geosciences

AIMS Geosciences, 11(1): 47–67.
DOI: 10.3934/geosci.2025004
Received: 23 October 2024
Revised: 20 December 2024
Accepted: 08 February 2025
Published: 13 February 2025

https://www.aimspress.com/journal/geosciences

Research article

Seismic response of utility tunnel systems embedded in a horizontal heterogeneous domain subjected to oblique incident SV-wave

Hui-yue Wang[1], Sha-sha Yu[1], De-long Huang[1,*], Chang-lu Xu[1], Hang Cen[1], Qiang Liu[2], Zhong-ling Zong[1] and Zi-Yuan Huang[3]

[1] School of Civil and Ocean Engineering, Jiangsu Ocean University, Lianyungang 222005, China
[2] Institute of Smart City and Intelligent Transportation, Southwest Jiaotong University, Chengdu 611756, China
[3] School of Civil Engineering, Harbin Institute of Technology, Harbin 150090, China

* **Correspondence:** Email: huangdl@jou.edu.cn.

Abstract: A horizontal non-homogeneous field adversely affects the seismic resistance of both the utility tunnel and its internal pipes, with seismic waves obliquely incident on the underground structure causing more significant damages. To address these issues, this study, based on a viscous-spring artificial boundary, derives and validates the equivalent junction force formula for the horizontal non-homogeneous field. It then establishes a three-dimensional finite element model of the utility tunnel, pipes, and surrounding soil to obtain the acceleration and strain responses of the utility tunnel and its internal pipes under seismic loading. Finally, it investigates the impact of different incidence angles of shear waves (SV waves) on the response of the utility tunnel and its internal pipes. It was found that as the PGA increases from 0.1 to 0.4 *g*, both peak acceleration and strain of the utility tunnel and its internal pipes increase. The peak acceleration of the utility tunnel and pipes initially decreases and then increases with the angle of incidence, while the strain increases with the angle of incidence, reaching its peak value when the angle of incidence is 30°. The acceleration and strain responses of the utility tunnel and pipe are higher in sand than in clay, with the peak acceleration strongly correlating with the angle of incidence of ground shaking. The findings of this study provide valuable insights into the seismic design of horizontal non-homogeneous field utility tunnel systems.

Keywords: utility tunnel; SV wave oblique incidence; horizontal non-homogeneous field; internal pipe

1. Introduction

In recent years, the promotion of sustainable policies has led to the rapid development of underground public infrastructure. However, this growth has also introduced various urban challenges, such as the overlapping of water and sewage pipes, power lines, and telecommunication cables, resulting in overcrowding of underground spaces and complicating the management and maintenance of municipal pipelines. Municipal engineers refer to this issue as the "spaghetti underground problem" [1]. A utility tunnel is a system of underground structures containing one or more public utilities allowing their renewal, maintenance, repair, and modification without excavation [2]. Utility tunnels provide ample shallow underground space, particularly vertical space, to prevent interference among underground public utility infrastructures and to provide sufficient space for new public utilities, fulfilling the requirement of sustainable development of underground space [3].

In the past, it was commonly assumed that utility tunnel systems were as seismically resistant as traditional tunnels. However, recent decades have revealed significant seismic damage to utility tunnel systems during major earthquakes, indicating their vulnerability [4]. In recent years, scholars both domestically and internationally have conducted a series of experimental studies [5,6] and numerical simulation analyses [7,8] on the seismic resistance of underground structures. Yu et al. [9] investigated semi-wireless long tunnels in two distinct horizontal regions by deriving simplified analytical solutions. The results revealed that the stress and deformation of mountain tunnels were more pronounced at the junction of soft and hard rocks. Zhang et al. [10] examined the longitudinal response of shield tunnels traversing soft and hard rocks and found that tunnel nodal displacements and internal forces in the lining were significantly increased near the interface of these rock types. Through in-depth studies of underground structural systems, it has been found that oblique ground vibration incidence is more damaging to underground structures than vertical incidence [11,12]. Panji et al. [13] investigated the linear ripple orthotropic anisotropic sublayer model using the half-space time-domain boundary element method (TD-BEM) and found that the method is influenced by the oblique incidence of planar SH waves, with wave propagation directly affecting geometric and material factors. Kavandi et al. [14] conducted a transient analysis of the SH wave scattering problem by proposing the dual reciprocal boundary element method (DR-BEM) and compared it with the method proposed by Panji. They showed that this method reduces model analysis time and can be used to prepare semi-space models in the field of geotechnical earthquake engineering. Mojtabazadeh et al. [15,16] proposed a new attenuated orthogonal anisotropic time-domain boundary element method to analyze the SH wave scattering problem. This method efficiently solves the SH wave scattering problem by introducing the mirror theory of the source and the Barkan attenuation method and can be applied to the seismic response of different geological structures. Li et al. [17,18] investigated the dynamic response of karst cavities with varying sizes and spans to shield tunnels under the influence of SV waves at different incident angles and demonstrated that structural displacements and stresses increase with the increase in the incident angle. Zarzalejos et al. [19] proposed oblique incident wave formulas for SV, SH, and P waves and applied them to frequency-domain boundary finite element models. They found that the structural bending moments under the action of ground-shaking oblique incident waves are significantly larger than those caused by vertical incidence. Huang et al. [20] investigated the effect of incident angles of SV and SH waves on the seismic response of long tunnels through numerical simulation. They demonstrated that the seismic response is more significantly influenced by the incident angle of S waves, with the effect intensifying as the incident angle increases. For non-uniform soils, Ye et al. [21] used the P2Psand model and a practical hysteresis model to simulate liquefiable sand and soft clay, respectively. They found that nodal displacements and lining stresses were

significant in shield tunnels near the interface of liquefiable sand and soft clay. Yan et al. [22] used a two-dimensional transient dynamic finite element technique to investigate the seismic response of layered soil-structure systems under an oblique incidence of P and SV waves. Results showed that oblique incidence significantly affects tunnel response, with the junction of the two soil layers being the most unfavorable location.

The aforementioned studies primarily focus on the angle of ground vibration incidence (vertical or oblique), layered soils, and horizontal non-homogeneous soils. However, limited research has been conducted on the response of utility tunnels and their internal pipes to oblique incident horizontal non-homogeneous field vibrations. In contrast to previous research, this paper establishes a viscous-spring artificial boundary and derives the three-dimensional oblique incidence formula for SV waves in non-uniform fields. Additionally, a static and dynamic analysis plug-in is developed for horizontal non-homogeneous soils using ABAQUS and Python. The study investigates the dynamic response of utility tunnels and internal pipes to oblique SV wave incidence in horizontal non-homogeneous fields, providing valuable references for seismic design, pipe support design, and vibration isolation. This work will serve as a reference for the seismic design of utility tunnels and their internal pipes.

2. Basic theory of oblique incidence of SV waves

2.1. Viscous-spring artificial boundary

Viscous-spring artificial boundaries effectively mitigate issues related to low-frequency drift and high-frequency instability, making them essential for simulating fluctuations in infinite domains [23]. The stress state expression at the node is as follows [24]:

$$\sigma_i(t) = \sigma_f(x, y, t) + c\dot{u}_f(x, y, t) + ku_f(x, y, t) \tag{1}$$

where $\sigma_i(t)$ denotes the equivalent load of a point *i* on the boundary at the moment t, $\sigma_f(x, y, t)$ is the stress generated by the original free field, $\dot{u}_f(x, y, t)$ and $u_f(x, y, t)$ are the free-field velocity and displacement of point i, respectively, and k and c values denote the elasticity coefficient and damping coefficient at the node, respectively, with different artificial boundary properties being simulated by different assignments to *k* and *c* values. The three-dimensional viscous-spring artificial boundary is shown in Figure 1. Eqs. (2) and (3) are the formulas for calculating the parameters of the three-way spring-damping element at the boundary node [25].

$$K_{BT} = a_T \frac{G}{R}, C_{BT} = \rho c_s \tag{2}$$

$$K_{BN} = \alpha_N \frac{G}{R}, C_{BN} = \rho c_p \tag{3}$$

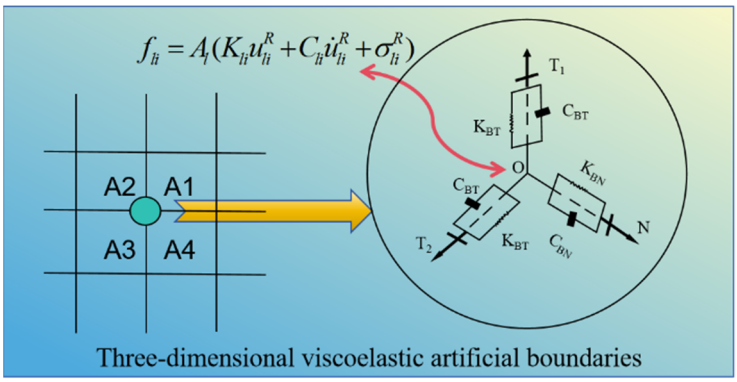

Figure 1. Spring damping model of viscous-spring artificial.

where K_{BN} and K_{BT} are the normal and tangential stiffness coefficients of the equivalent spring, respectively; C_{BN} and K_{BT} are the normal and tangential damping coefficients of the equivalent damper, respectively; c_s and c_p are the shear and compression wave velocities of the medium, respectively; G is the shear modulus of the medium; ρ is the density of the medium; and α_N and α_T are the correction coefficients for the normal and tangential viscous-spring artificial boundary, respectively, which are taken concerning the recommended values by Liu [26] (see Table 1).

Table 1. Spring correction factor.

Group	Parameter	Value range	Recommended value
Two-dimensional	α_T	0.35–0.65	1/2
	α_N	0.8–1.2	2/2
Three-dimensional	α_T	0.5–1.0	2/3
	α_N	1.0–2.0	4/3

2.2. Horizontal non-homogeneous field equivalent nodal force

The application of ground vibration is realized by the equivalent nodal force on the viscous-spring artificial boundary nodes, which mainly consists of three parts. The first two parts are ku_f and $c\dot{u}_f$, whose function is to eliminate the hindering effect of the artificial boundary on the soil body; ku_f eliminates the role of the spring of the viscous-spring artificial boundary; $c\dot{u}_f$ eliminates the role of the damper; and σ_f is the free-field motion on the surface of the artificial boundary produced by shear stresses, which is calculated by the formula [27]:

$$F_B = (\sigma_f + ku_f + c\dot{u}_f)A \tag{4}$$

where A is the effective area represented by the artificial boundary points; Eq. (3) is used to calculate the equivalent nodal force load at the boundary nodes. It should be noted that when the SV wave is incident at an angle lower than a certain value, there will be both reflected SV waves and refracted P waves at the soil demarcation interface. On the other hand, when the SV wave is incident at an angle greater than a certain value, there will only be reflected SV waves at the soil demarcation surface of the SV wave; this angle is called the critical angle of incidence. According to Snell's law, it is calculated

by the following equation [28]:

$$\theta_{cr} = \arcsin\left(\frac{c_s}{c_p}\right) = \arcsin\left(\sqrt{\frac{1-2v}{2(1-v)}}\right) \tag{5}$$

where v is the Poisson's ratio of the soil. The spatial incidence diagram of the SV wave is shown in Figure 2, where the angle between the incident direction and the z-axis is α, and the angle between the incident direction and the y-axis is β. The incident SV wave undergoes a wave conversion at the interface of the medium, which produces the SV wave with the reflecting angle of β and the P wave with the refracting angle of γ.

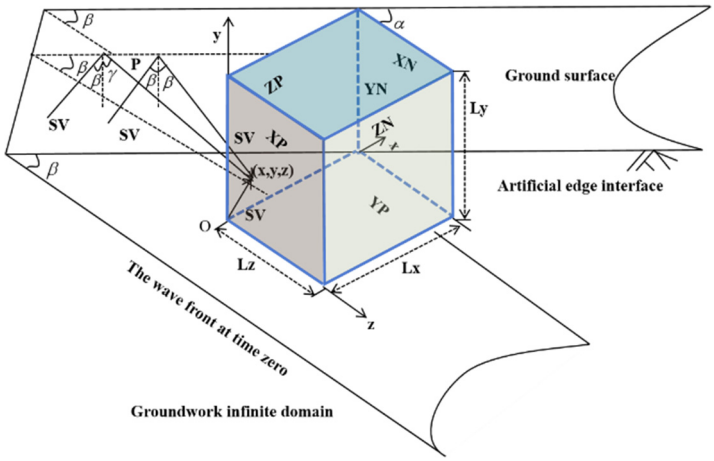

Figure 2. Schematic diagram of three-dimensional oblique incidence.

In this paper, we study the effect of oblique incidence of non-homogeneous field SV waves on the response of a structural system with a free field as shown in Figure 3.

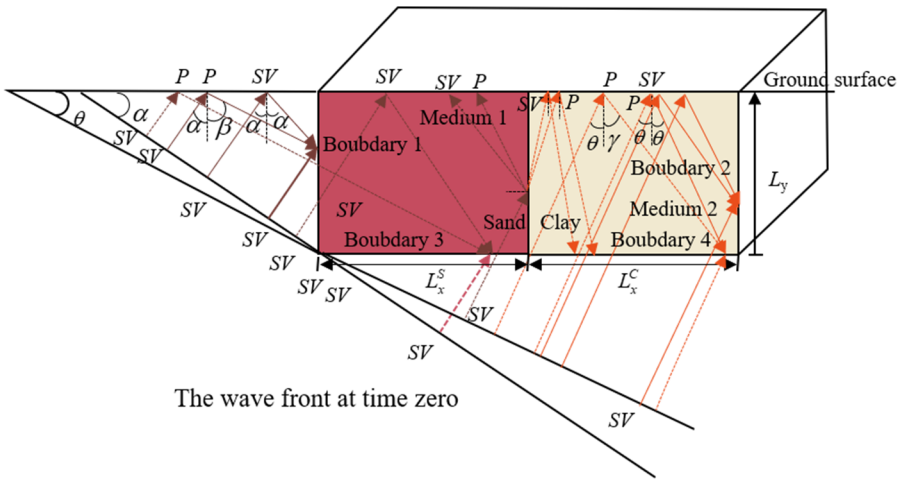

Figure 3. Schematic diagram of two-dimensional oblique incidence of SV wave in a horizontal non-homogeneous field.

To calculate the equivalent nodal force, the delay time required for each wave to the truncated surface is calculated first, and Δt_1, Δt_2, and Δt_3 denote the delay time for the incident SV wave, the

reflected SV wave, and the reflected P wave on the left boundary, respectively, as follows:

$$\begin{cases} \Delta t_1 = \dfrac{y\cos\alpha}{c_s^1} \\ \Delta t_2 = \dfrac{(2L_y - y)\cos\alpha}{c_s^1} \\ \Delta t_3 = \dfrac{[L_y - (L_y - y)\tan\alpha\tan\beta]\cos\alpha}{c_s^1} + \dfrac{L_y - y}{c_p^1\cos\beta} \end{cases} \tag{6}$$

where L_y is the length of the truncated body on the y-axis; *x*, *y* are the coordinates of the nodes; and c_s^1 and c_p^2 are the shear and compressional wave speeds of the sand, respectively. For the delay time of each wave at the right boundary, since the SV wave passes through a different medium, the SV wave scattering angle is considered to be θ, and the P wave scattering angle is γ, which are calculated according to Eq. (7) [28]:

$$\frac{\sin\theta_{rs}}{c_s^1} = \frac{\sin\theta_{ts}}{c_s^2} \tag{7}$$

where r and t represent reflected and transmitted waves, respectively; and c_s^2 represents the shear wave velocity of the medium

The stresses at boundary 2 can be calculated for each equivalent node based on the free-field displacement equation:

$$\begin{cases} \sigma_x = \dfrac{G_1}{c_s^1}\sin 2\alpha\left(\dot{u}_1\left(t-\Delta t_1\right) - B_1\dot{u}_2\left(t-\Delta t_2\right)\right) + \\ \quad B_2\dfrac{\lambda + 2G_1\sin^2\beta}{c_p^1}\dot{u}_3\left(t-\Delta t_3\right) \\ \sigma_y = \dfrac{G_1}{c_s^1}\cos 2\alpha\left(u_1\left(t-\Delta t_1\right) + B_1\dot{u}_2\left(t-\Delta t_2\right)\right) - \\ \quad B_2\dfrac{G_1\sin 2\beta}{c_p^1}\dot{u}_3\left(t-\Delta t_3\right) \end{cases} \tag{8}$$

where $\dot{u}_1(t-\Delta t_1)$, $\dot{u}_2(t-\Delta t_2)$, and $\dot{u}_3(t-\Delta t_3)$ are the velocities in the *x*, *y*, and *z* directions, respectively; and G_1 is the medium 1 shear modulus. The same boundary 1 stress equation is:

$$\begin{cases} \sigma_x = \dfrac{G_2}{c_s^2}\sin 2\theta\left(\dot{u}_4\left(t-\Delta t_4\right) - B_3\dot{u}_5\left(t-\Delta t_5\right)\right) + \\ \quad B_4\dfrac{\lambda + 2G_2\sin^2\gamma}{c_p^2}\dot{u}_6\left(t-\Delta t_6\right) \\ \sigma_y = \dfrac{G_2}{c_s^2}\cos 2\theta\left(u_4\left(t-\Delta t_4\right) + B_3\dot{u}_5\left(t-\Delta t_5\right)\right) - \\ \quad B_4\dfrac{G_2\sin 2\gamma}{c_p^2}\dot{u}_6\left(t-\Delta t_6\right) \end{cases} \tag{9}$$

where G_2 is the shear modulus of medium 2. Similarly, the stress equation for the bottom boundary 3 in medium 1 is calculated as follows:

$$\begin{cases} \sigma_x = \dfrac{G_1}{c_s^1}\cos 2\alpha\left(\dot{u}_7\left(t-\Delta t_7\right)+B_1\dot{u}_8\left(t-\Delta t_8\right)\right)- \\ \quad B_2\dfrac{G_1\sin 2\beta}{c_p^1}\dot{u}_9\left(t-\Delta t_9\right) \\ \sigma_y = \dfrac{G_1}{c_s^1}\sin 2\alpha\left(-\dot{u}_7\left(t-\Delta t_7\right)+B_1\dot{u}_8\left(t-\Delta t_8\right)\right)+ \\ \quad B_2\dfrac{\lambda+2G_1\cos^2\beta}{c_p^1}\dot{u}_9\left(t-\Delta t_9\right) \end{cases} \tag{10}$$

The stress equation for boundary 4 in medium 2 is calculated as follows:

$$\begin{cases} \sigma_x = \dfrac{G_2}{c_s^2}\sin 2\theta\left(\dot{u}_{10}\left(t-\Delta t_{10}\right)-B_3\dot{u}_{11}\left(t-\Delta t_{11}\right)\right)+ \\ \quad B_4\dfrac{\lambda+2G_2\sin^2\gamma}{c_p^2}\dot{u}_{12}\left(t-\Delta t_{12}\right) \\ \sigma_y = \dfrac{G_2}{c_s^2}\cos 2\theta\left(\dot{u}_{10}\left(t-\Delta t_{10}\right)+B_3\dot{u}_{11}\left(t-\Delta t_{11}\right)\right)- \\ \quad B_4\dfrac{G_2\sin 2\gamma}{c_p^2}\dot{u}_{12}\left(t-\Delta t_{12}\right) \end{cases} \tag{11}$$

Finally, the displacement, velocity, and stress equations on the corresponding surfaces are substituted into Eq. (4) to obtain the corresponding equivalent nodal loads.

3. Utility tunnel testing and numerical modeling

3.1. Utility tunnel testing

The vibration table test for the utility tunnel was conducted at the Structure and Seismic Experiment Center of Harbin Institute of Technology. The vibration table provides unidirectional horizontal vibration, with a table size of 4000 mm × 3000 mm, a maximum horizontal displacement of ±125 mm, a maximum acceleration of ±1.5 *g*, and a load capacity of 12 tons. The design of the stacked shear box considers the geometry of the utility tunnel, the dimensions of the vibration table, and its load capacity. The internal dimensions of the shear box are 1900 mm × 1400 mm × 1570 mm.

In this test, Buckingham's theorem was applied to determine the model similarity ratio, ensuring that the seismic response of the model accurately reflects the behavior of the utility tunnel prototype. Considering the capacity of the shaking table and the size of the model box, the cross-sectional dimensions of the prototype utility tunnel are reduced from 7000 mm × 6000 mm to 700 mm × 600 mm, with a length similarity ratio of 1/10. The model was constructed using 2 mm diameter wire and concrete, with a modulus of elasticity similarity ratio of 1 and an acceleration similarity ratio of 2. The overall dimensions of the utility tunnel model are 1800 mm × 700 mm × 600 mm, with a wall thickness of 40 mm. Three pipes were laid inside the utility tunnel: cast iron pipes P-A, P-B, and P-C were positioned at the bottom of the large chamber, the side wall, and the bottom of the small chamber, respectively. The pipes have a length of 1800 mm, an outer diameter of 60 mm, and a wall thickness of 3.5 mm, while the prototype pipes are made of ductile iron.

3.2. Validation of ground vibration effectiveness

This paper develops a horizontal non-consistent field input program based on Python to implement the application of equivalent seismic loads and viscous-spring artificial boundaries in ABAQUS finite element software. The details are as follows:

(1) Establish the utility tunnel–soil model, retrieve node information using the plug-in, and iteratively perform the static ground stress equilibrium via the CSV file to output the static boundary node reaction forces;

(2) Calculate the static boundary node information using the plug-in and apply the viscous-spring artificial boundary according to Eqs. (2)–(3);

(3) After applying the artificial boundary, select the ODB file from the penultimate iteration of the CSV file, perform the dynamic ground stress equilibrium, apply the boundary node reaction forces, and convert the static boundary into the dynamic boundary;

(4) Using Eqs. (4)–(11), use the plug-in to calculate the equivalent seismic loads at different angles and apply them to the model;

(5) Finally, create the task, modify the INP file, define the initial conditions as *initial conditions, type = stress, input = soil.csv, and submit the task. The specific steps are shown in Figure 4.

A numerical model is established to verify the simulation accuracy of the oblique incidence method of SV waves in a horizontal non-homogeneous field. A finite element model of size 1000 × 500 × 200 m is selected, with a grid size of 20 m. The density of the medium on both sides of the finite element model is 2500 kg/m³, with a Poisson's ratio of 0.3. The modulus of elasticity for the left medium is 3 GPa, while for the right medium, it is 1.5 GPa. Observation points A and B are selected (see Figure 5). A pulsed wave with a duration of 0.25 s is used as the incident wave, with its displacement and velocity-time curves shown in Figure 6, calculated as [29]:

$$A_{SV}(t)=16A[z(\frac{t}{T})-4z(\frac{t}{T}-\frac{1}{4})+6z(\frac{t}{T}-\frac{1}{2})-4z(\frac{t}{T}-\frac{3}{4})+z(\frac{t}{T}-1)] \tag{12}$$

where $A=1$, $Z(a)=a^3H(a)$, and $H(a)$ is the Heaviside function ($H(a)=0$ when $a<0$; $k=1$ and $H(a)=1$, when $a\geq 0$, $a=\frac{t}{T}$).

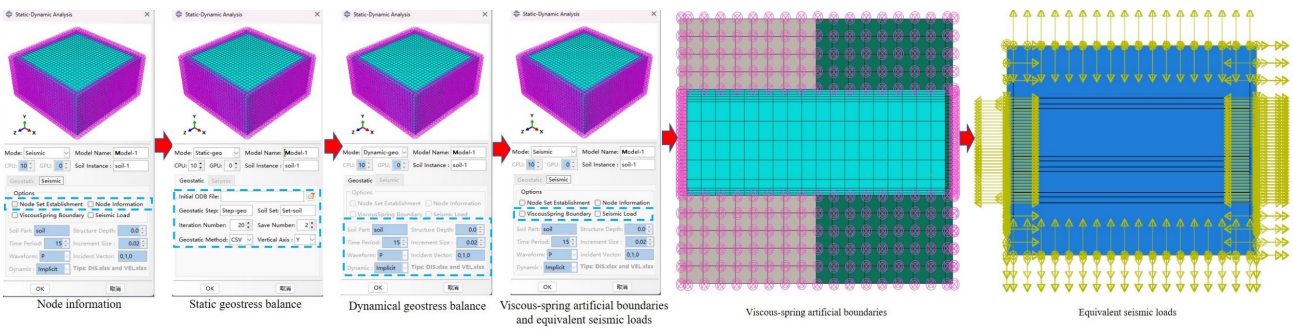

Figure 4. Python plug-in in ABAQUS.

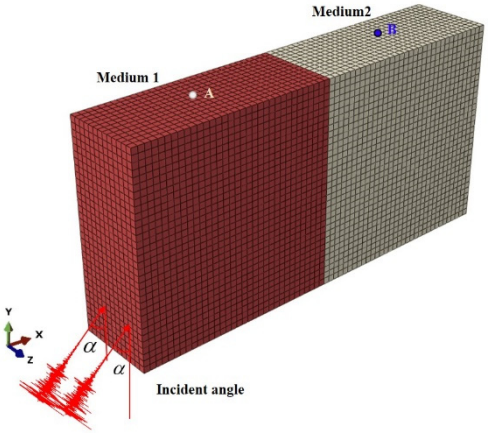

Figure 5. Validated model.

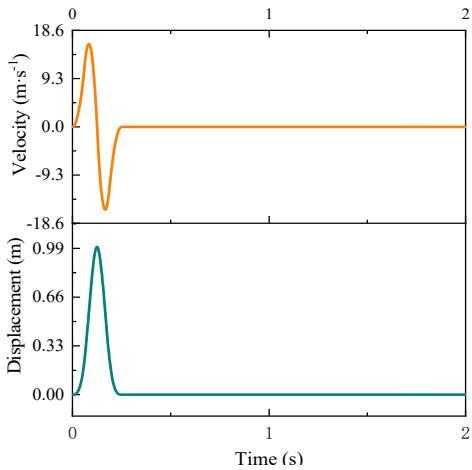

Figure 6. Displacement and velocity history of incident SV wave.

The time-history curves of vertical and horizontal displacements at points A and B at the top of the medium, as shown in Figure 5, are presented in Figure 7. The numerical and analytical solution results align well, indicating that the method presented in this paper effectively studies SV wave propagation in sand and clay.

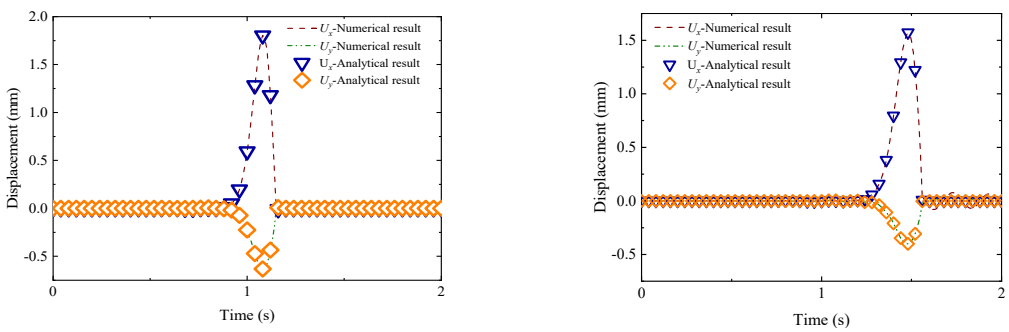

(a) Point A (b) Point B

Figure 7. Observation point of vertical and horizontal displacement time history curves.

3.3. Finite element modeling

A utility tunnel–pipe–soil model is established using ABAQUS finite element software, with dimensions consistent with the experimental setup. Three pipes are placed within the utility tunnel: cast iron pipes P-A, P-B, and P-C are positioned at the bottom of the large chamber, the side wall, and the bottom of the small chamber, respectively. Pipe P-A is supported by concrete piers, pipe P-B is restrained by an angle support, and pipe P-C is placed directly in the small chamber groove. The model is shown in Figure 8.

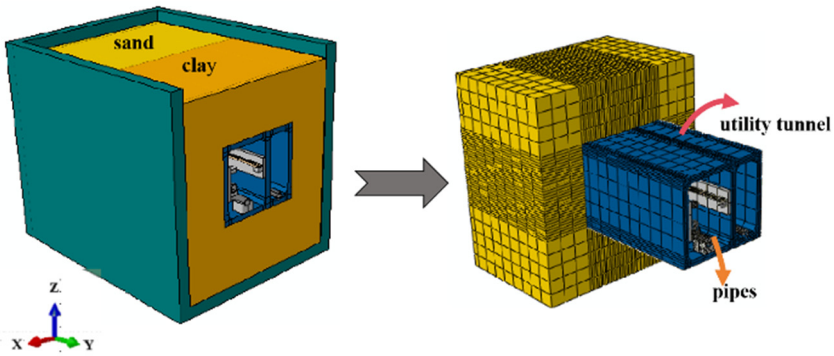

Figure 8. Finite element model.

3.3.1. Model material properties

Both clay and sand were modeled using the Mohr-Coulomb constitutive model. The utility tunnel was constructed with C35 concrete, employing the concrete plastic damage model [30]; HRB400 steel reinforcement was used, with the bond-slip effect between the reinforcement bars not considered in the model. The reinforcement bars were modeled using T3D2 two-node linear elements, and the material parameters were used from experimental data and are shown in Table 2.

Table 2. Material parameter.

Parameter	Materials			
	Concrete	Steel bar	Sand	Clay
Elastic modulus (GPa)	0.021	207	0.05	0.02
Poisson's ratio	0.2	0.25	0.3	0.3
Friction angle (°)	32	-	32	20
Eccentricity/yield strength (MPa)	0.1	0.235	-	-
Axial compression ratio/cohesion (kPa)	1.16	-	0	5
K (stiffness matrix)	0.67	-	-	-
Density (kg/m^3)	2300	7800	1692	1430

The structural formula for spring and damping at the boundary is crucial for implementing the viscous-spring artificial boundary. In this paper, Rayleigh damping is employed to achieve more accurate numerical simulation results, calculated as follows [31]:

$$C = \alpha M + \beta K \tag{13}$$

where α and β are the proportionality constants of the mass and stiffness matrices, calculated using the following equations:

$$\xi_{\min} = (\alpha\beta)^{1/2} \tag{14}$$

$$\omega_{\min} = (\alpha / \beta)^{1/2} \tag{15}$$

where $\xi_{\min}$ is the minimum damping ratio of soil, taken as 0.05 in this paper, and $\omega_{\min}$ is the main frequency of seismic wave input. In this paper, based on the test soil parameters, the finite element model has a sand damping coefficient α of 0.402 and β of 0.005, and a clay damping coefficient α of 0.497 and β of 0.005.

3.3.2. Mesh division

C3D8R elements are used for the soil, utility tunnel, pipe, and support grid cells, while truss elements are used to model the reinforcement. The cell size affects both convergence and the accuracy of the results. According to Lysmer et al. [32], the model grid size should be determined using the following equation:

$$l_e < \frac{1}{8}\lambda_s = \frac{1}{8f_{\max}} v_s \tag{16}$$

where l_e is the model mesh size; λ_s and v_s are the wavelength and shear wave velocity of seismic waves, respectively; and $f_{\max}$ is the maximum frequency of seismic waves.

In this study, the maximum frequency of input ground vibration is 2.5 Hz, and the minimum transverse wave velocity is 42 m/s, resulting in a maximum grid size of $l_e <$ 2.1 m. To ensure the accuracy of the calculations, the maximum grid size is 0.1125 m for the soil body, 0.11 m for the utility tunnel, and 0.05 m for the pipe. To ensure a more realistic contact between the soil body and the utility tunnel, the minimum grid size for the utility tunnel is 0.015 m, which is larger than the surrounding soil body cells.

3.3.3. Contact settings

In the finite element model, interactions between the soil body and the utility tunnel are considered, with the two set to face-to-face contact. Hard contact is applied in the normal direction, and the tangential direction is governed by a *penalty factor* with a friction coefficient of 0.4. Face-to-face contact is established between the pipe and its corresponding support, accounting for the material surface roughness characteristics. The friction coefficient is set to 0.4 for the convenience of the study. Binding constraints are used between each support and the utility tunnel wall.

3.4. Seismic wave loading

The El-Centro wave is selected as the input wave, with the ground shaking time course and Fourier spectrum shown in Figure 9, featuring a predominant frequency of 2.5 Hz. The acceleration was amplitude-modulated to 0.1 (small earthquake), 0.2 (medium earthquake), and 0.4 *g* (large earthquake) based on the PGA values. For each PGA, different working conditions were applied, with angles of 0°, 5°, 10°, 15°, 20°, 25°, and 30° for the SV wave in the xy plane. The incident angle A was defined as the angle between the incident direction and the y-axis.

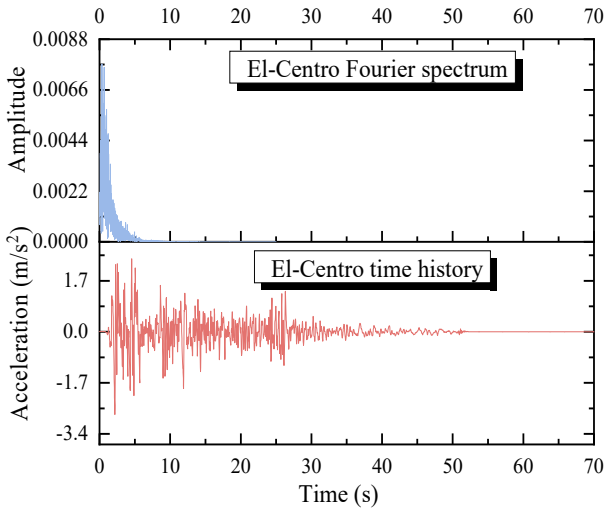

Figure 9. Time history curves and Fourier spectrum curves of the El-Centro wave.

4. Acceleration dynamic response of SV wave longitudinal oblique incidence utility tunnel system

4.1. Peak acceleration of the utility tunnel

Figure 10 shows the peak acceleration of the utility tunnel under El-Centro waves and the acceleration time profile at PGA = 0.4 *g*. Figure 10(a) and (b) show the peak acceleration on the upper side of the utility tunnel (at data collection points A2 and A3), while Figure 10(c) and (d) display the peak acceleration on the lower side (at data collection points A1 and A2). It is observed that the peak acceleration increases with the PGA, exhibiting a trend of first decreasing and then increasing with the incident angle. The acceleration is smallest at an incident angle of 25°, reaching its maximum at an incident angle of 30°. This is because the critical angle of incidence for the SV wave under the conditions of this study is 25°. When the angle of incidence exceeds this value, the reflected P-wave primarily manifests as a surface wave, increasing the horizontal acceleration. This finding is consistent with the conclusions of Xu et al. [33]. Figure 11 presents the acceleration cloud diagram of the utility tunnel, where it can be observed that the acceleration on the upper side of the utility tunnel is greater than that on the lower side. This is due to the fact that structural acceleration generally decreases with increasing burial depth, a trend also observed in the study by Wang et al. [34].

It can also be observed that, on the upper side of the utility tunnel in the sand, when PGA = 0.1 *g*, the difference in peak acceleration between incidence angles of 0° and 30° is 0.074 m/s². When PGA = 0.4 *g*, the difference increases to 0.191 m/s². On the upper side of the utility tunnel in the clay, when PGA = 0.1 *g*, the difference in peak acceleration between 0° and 30° is 0.037 m/s². When PGA = 0.4 *g*, the difference increases to 0.131 m/s². This suggests that the utility tunnel response is more sensitive to the incident angle at higher PGA than at lower PGA. The difference between the peak values in the sand is greater than in the clay, and this phenomenon also occurs on the lower side of the utility tunnel, although the difference is smaller compared to that on the upper side. It can also be observed that the peak acceleration response in the sand is greater than in the clay, which can be attributed to the higher cohesive force of clay compared to sand, resulting in greater energy dissipation from ground shaking. This also suggests that sand is more sensitive to the oblique incidence of ground shaking. The time-range plot shows that the peak acceleration distribution region of the utility tunnel closely aligns with

the El-Centro wave time-range curve, suggesting that the dynamic response of the utility tunnel is influenced by the type of seismic wave. Additionally, the figure shows that the test results align well with the finite element results, with the difference being within 15%. This indicates that the finite element model presented in this study demonstrates a certain degree of reliability.

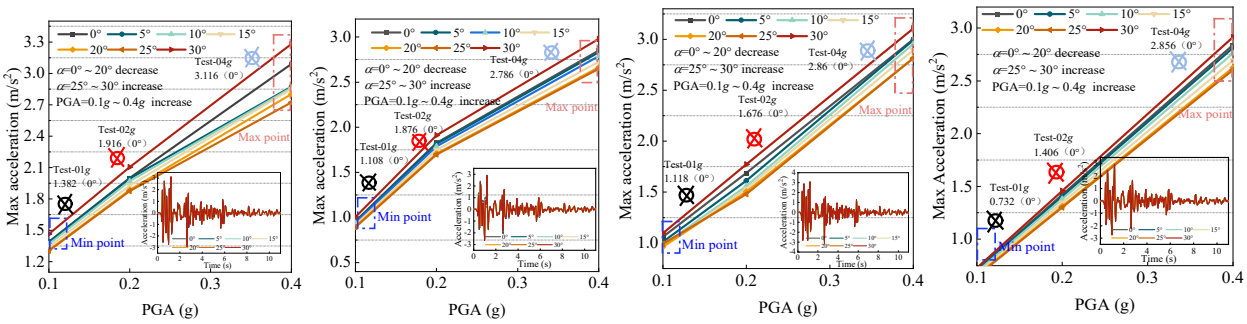

(a) Sand (El-Centro, above) (b) Clay (El-Centro, above) (c) Sand (El-Centro, under) (d) Clay (El-Centro, under)

Figure 10. Peak response of x-direction acceleration of different soils (above and under the utility tunnel).

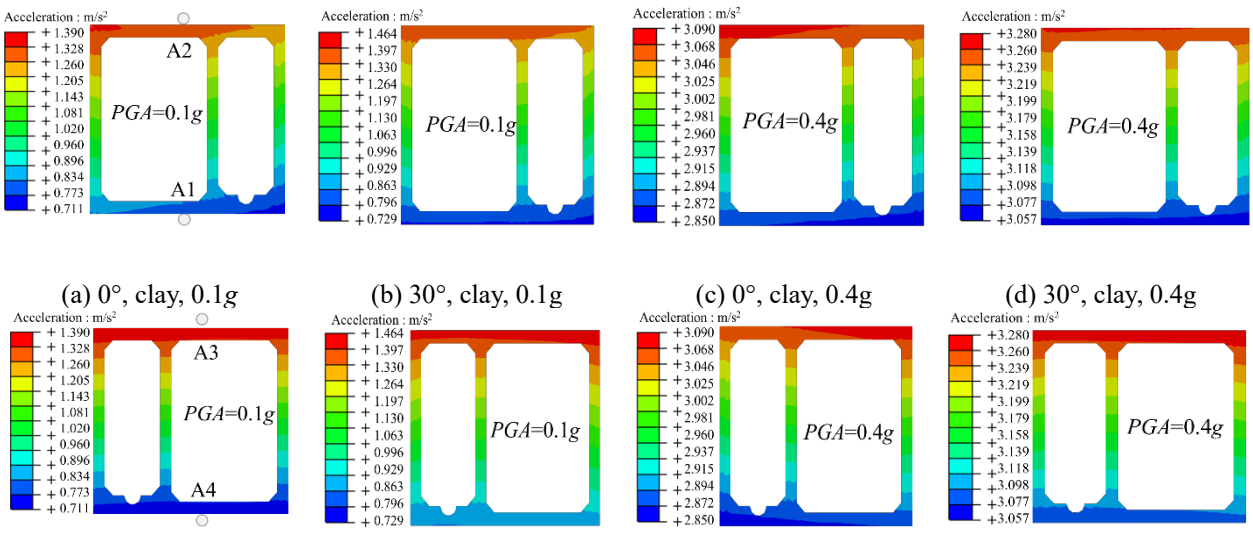

(a) 0°, clay, 0.1*g* (b) 30°, clay, 0.1g (c) 0°, clay, 0.4g (d) 30°, clay, 0.4g

(e) 0°, sand, 0.1*g* (f) 30°, sand, 0.1g (g) 0°, sand, 0.4g (h) 30°, sand, 0.4g

Figure 11. Acceleration cloud map of the utility tunnel with different soils and incident angles.

4.2. Peak pipe acceleration

Figure 12 shows the peak acceleration of pipes P-A and P-B subjected to the El-Centro wave, as well as the acceleration time history at a PGA of 0.4 *g*. The data collection points are A5–A8. It can be observed that the peak acceleration of the pipes follows the same trend as the peak acceleration in the utility tunnel, i.e., a decrease followed by an increase as the incidence angle increases. The maximum peak acceleration for both pipes P-A and P-B occurred early on, accompanied by larger fluctuations; this was due to the higher total energy of the El-Centro wave and its maximum frequency appearing in the initial phase. At this time, the supports of pipes P-A and P-B are subjected to more seismic energy, the support consumes part of the ground vibration energy, and the fluctuation of the pipe tends to be stabilized. By combining the peak acceleration of the pipe in Figure 12 and the acceleration cloud

diagram of the pipe in Figure 13, it can be observed that the peak acceleration of pipe P-A is greater than that of pipe P-B. As introduced in the previous section, pipe P-A is supported by concrete piers, while pipe P-B is restrained by an angle, indicating that the restraining capacity of the angle is superior to that of the concrete piers. The figure also shows that the peak acceleration of the pipe in the sand soil is greater than that in the clay, which follows the same pattern as the peak acceleration in the utility tunnel. A comparison of the experimental results with the finite element results reveals that the difference between the two is within 10%, suggesting that the simulation is reliable.

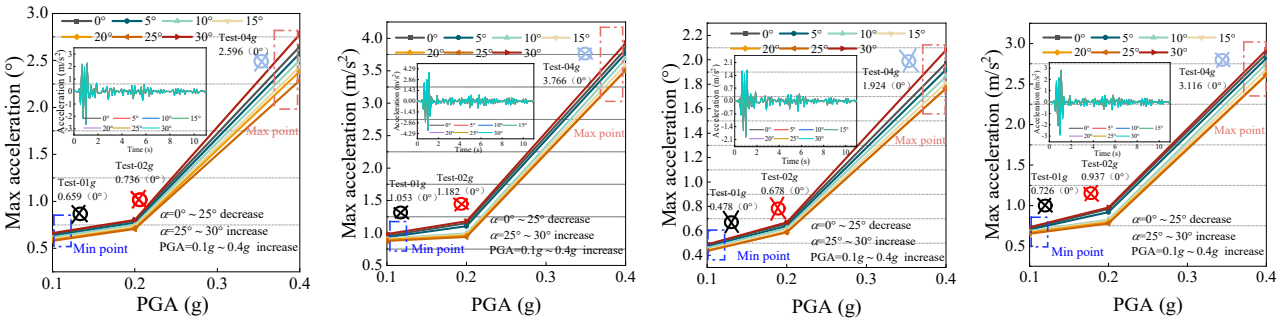

(a) Pipe P-A, clay (b) Pipe P-A, sand (c) Pipe P-B, clay (d) Pipe P-B, sand

Figure 12. Peak acceleration response of pipes P-A and P-B.

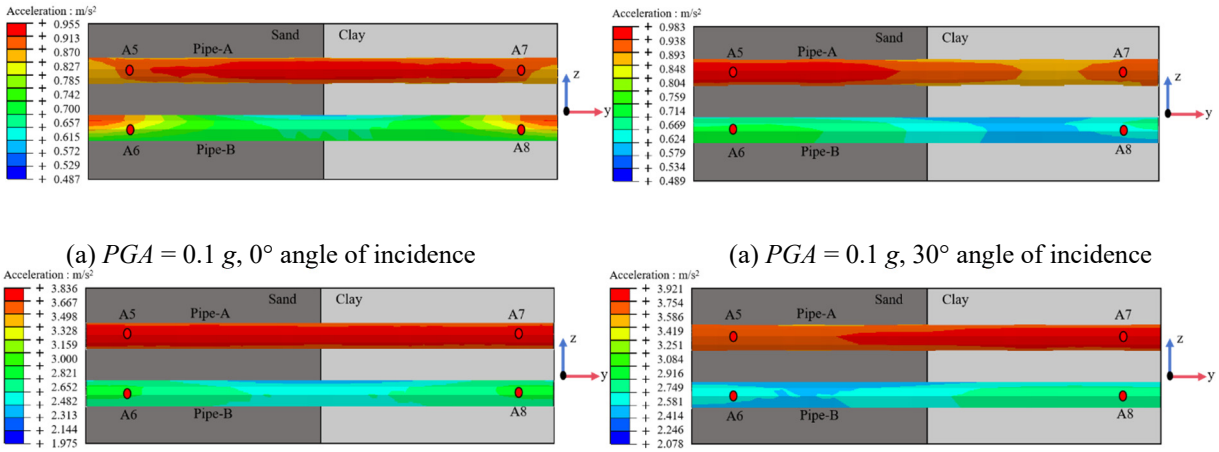

(a) *PGA* = 0.1 *g*, 0° angle of incidence (a) *PGA* = 0.1 *g*, 30° angle of incidence

(c) *PGA* = 0.4 *g*, 0° angle of incidence (d) *PGA* = 0.4 *g*, 30° angle of incidence

Figure 13. Acceleration cloud map of pipes with different soils and incident angles.

5. Strain response of SV wave longitudinal oblique incidence utility tunnel system

5.1. Utility tunnel peak strain

Figure 14 shows the peak axial strain curves of the El-Centro wave with varying PGA and incident angles at different locations along the utility tunnel in both sand and clay areas. It can be observed that the strains at both the upper and lower sides of the utility tunnel (data collection points S1–S4) increase as the incident angle (0°–30°) increases. This trend is observed in both sand and clay.

In the upper side of the utility tunnel in the sand, the peak strain increases by factors of 9.26, 13.34, and 16.51 as the incident angle increases for PGA of 0.1, 0.2, and 0.4 *g*, respectively. A similar trend is observed in clay, where the peak strain increases by 9.14, 12.43, and 15.82 times, respectively.

This suggests that the rate of strain growth is more influenced by PGA than by soil type. Additionally, the angle of incidence shows greater sensitivity to changes in PGA. For the peak strain on the lower side of the utility tunnel, the same trend is observed, but with a smaller growth rate compared to the upper side.

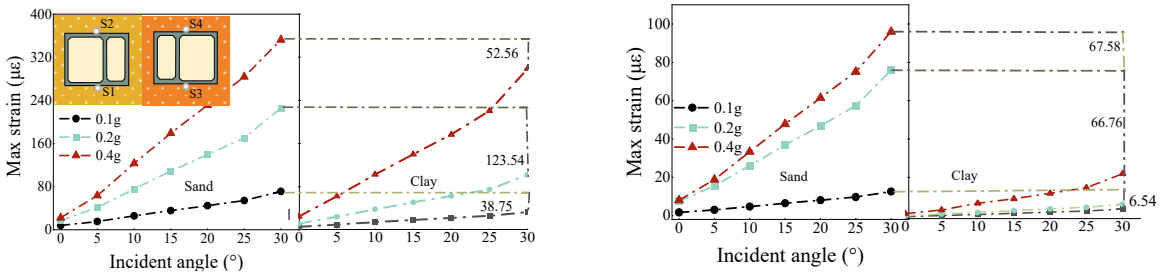

(a) Above side of utility tunnel (sand, clay) (b) Under the utility tunnel (sand, clay)

Figure 14. Peak strain curves for different soils (above and under the utility tunnel).

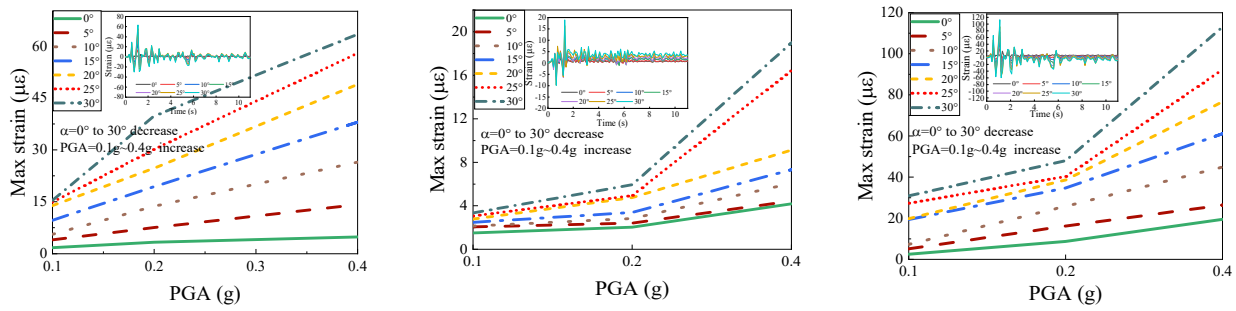

(a) Pipe P-A, P-B, P-C (Clay, El-Centro wave)

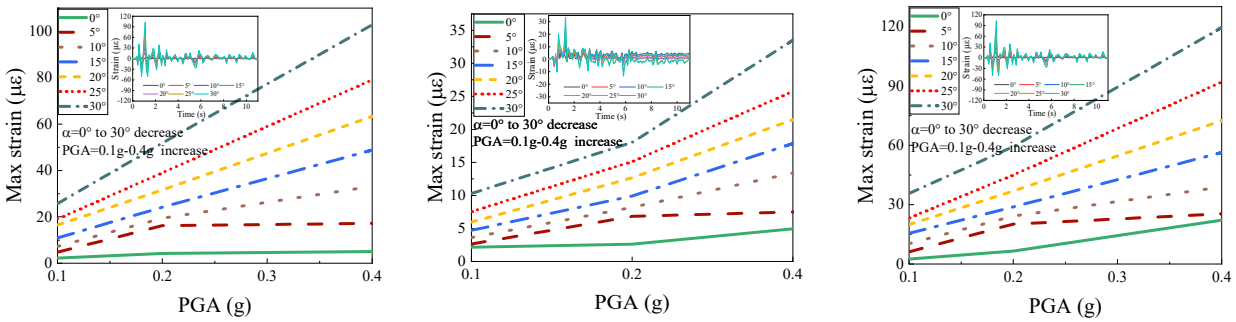

(b) Pipe P-A, P-B, P-C (Sand, El-Centro wave)

Figure 15. Strain response of pipes P-A, P-B, and P-C.

5.2. Peak pipe strain

Figure 15 shows the axial peak strain and time-range response of pipes P-A, P-B, and P-C. It can be observed that the peak strains of pipes P-A, P-B, and P-C increase with the incident angle. In the sand, with a PGA of 0.4 *g*, the peak strains of pipes P-A, P-B, and P-C are 63.39 με, 18.97 με, and 113.45 με at an incident angle of 30°, which represent increases of 20.29, 6.76, and 5.39 times compared to 0°, respectively. This indicates that pipe P-C experiences the largest deformation, followed by pipe P-A; pipe P-B shows the smallest deformation. This is attributed to the fact that pipe P-C is placed directly in the recess of the chamber without additional constraints, while pipe P-B is

constrained by an angle steel bearing and pipe P-A by a concrete bearing, resulting in the smallest deformation for pipe P-B. This further demonstrates that the restraining capacity of the angle bearing is superior to that of the concrete pier bearing, which is consistent with the acceleration study results presented in Section 4.2.

Both clay and sand exhibit a similar pattern, but the peak pipe strain and growth rate are higher in sand than in clay. This is partly due to sand being less damped than clay and is also influenced by the frequency of the El-Centro wave. Sand is more responsive to high-frequency seismic waves (above 1 Hz), whereas clay is more sensitive to lower frequencies. The El-Centro wave is a medium-to-high-frequency wave; as a result, it tends to cause resonance in the sand, leading to a more pronounced structural response. The strain-time response indicates that pipes P-A, P-B, and P-C exhibit significant deformation in the early stages, which aligns with the peak acceleration behavior of the pipes. This suggests that deformation is generally larger at moments of higher acceleration.

6. Discussion

6.1. Correlation between seismic wave incidence angle and peak acceleration of utility tunnel

Section 4.1 indicates that the peak acceleration of the utility tunnel and pipe exhibits a trend of first decreasing and then increasing with the incident angle velocity. This section further explores the correlation between the incident angle and peak acceleration. Based on the acceleration trend, a cubic polynomial is introduced to fit the incident angle and peak acceleration, with the calculated results serving as empirical formulas for practical engineering. The correlation coefficient R^2 reflects the degree of correlation between the two, and the fitting polynomial is:

$$y = B_1 x^3 + B_2 x^2 + B_3 x + Intercept \tag{17}$$

where B_1, B_2, B_3 are variable coefficients, x is the angle of incidence, y is the peak acceleration, and $Intercept$ is a constant.

Figure 16 shows the fitting curves of peak acceleration and ground shaking incidence angle for the utility tunnel. The fitting quality in the sand is superior to that in the clay, with correlation coefficients R^2 exceeding 0.9. This suggests that the oblique incidence of seismic waves more significantly influences peak acceleration in the sand. It can also be found that the values of B_1, B_2, and B_3 increase with the increase of PGA. Both clay and sand have the best fit at PGA = 0.2 *g*, indicating that the peak acceleration of the utility tunnel has the highest correlation with the angle of incidence of ground shaking at PGA = 0.2 *g*.

6.2. Correlation between seismic wave incidence angle and peak acceleration of pipe

From Figures 17 and 18, it is observed that there is a better fit of pipes P-A and P-B, with the correlation coefficients (R^2) exceeding 0.9. This indicates that the correlation between the peak acceleration of the pipeline and the angle of incidence is stronger than that of the utility tunnel, possibly because the utility tunnel provides a protective effect on the pipe, which is less affected by ground vibration. This results in a smoother relationship between the angles and acceleration. It is observed that the values of B_1, B_2, and B_3 increase with increasing PGA, and the pipe fits better in the sand than in the clay. Both clay and sand exhibit the best fit overall at PGA = 0.1 *g*, suggesting that the peak

acceleration of the pipe has the highest correlation with the angle of incidence of ground shaking at PGA = 0.1 *g*.

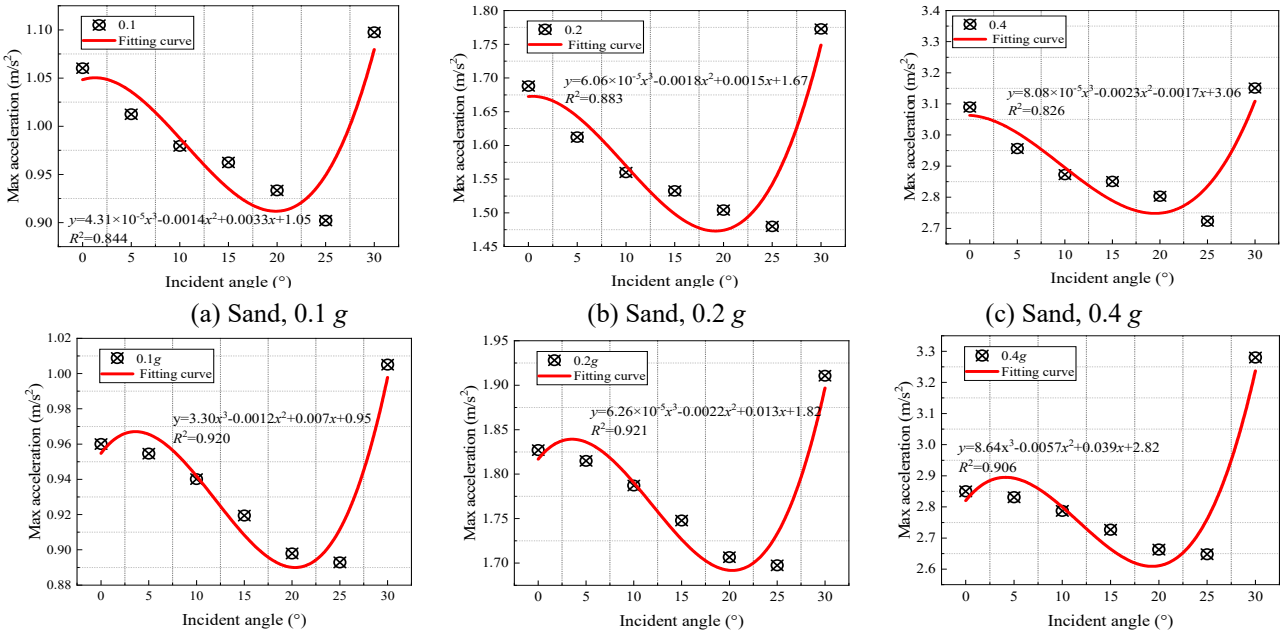

(a) Sand, 0.1 *g* (b) Sand, 0.2 *g* (c) Sand, 0.4 *g*

(d) Clay, 0.1 *g* (e) Clay, 0.2 *g* (f) Clay, 0.4 *g*

Figure 16. Fitted plot of incidence angle vs. correlation of peak acceleration in the utility tunnel.

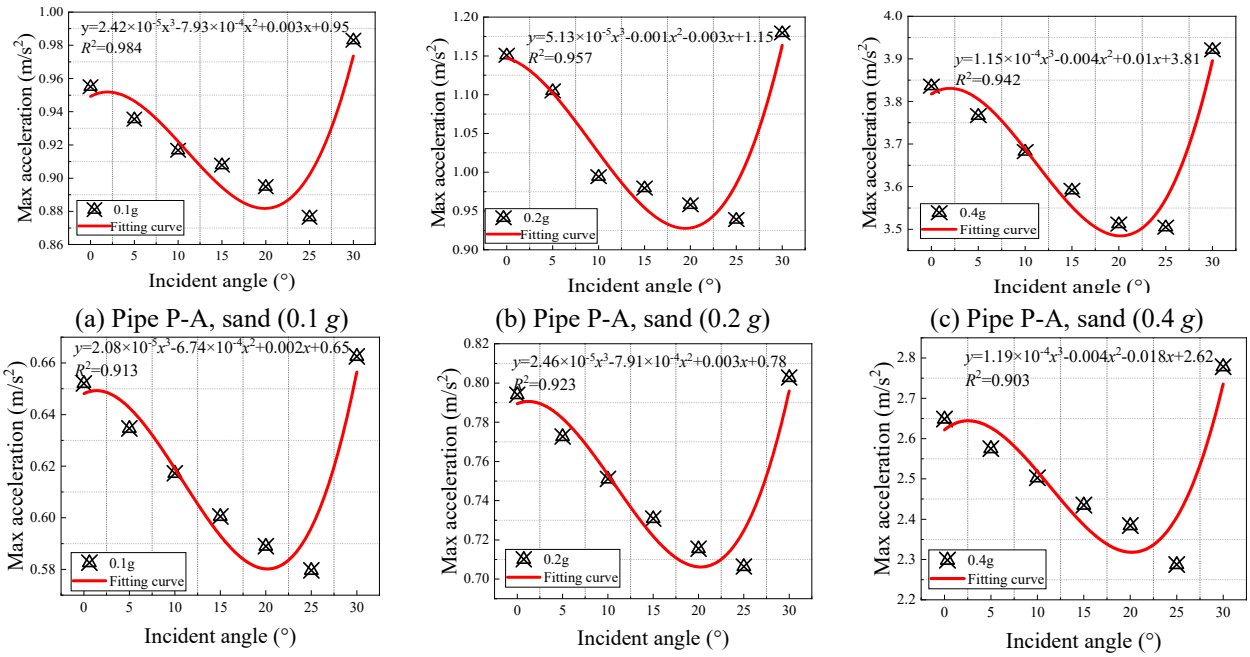

(a) Pipe P-A, sand (0.1 *g*) (b) Pipe P-A, sand (0.2 *g*) (c) Pipe P-A, sand (0.4 *g*)

(d) Pipe P-A, clay (0.1 *g*) (e) Pipe P-A, clay (0.2 *g*) (f) Pipe P-A, clay (0.4 *g*)

Figure 17. Correlation of pipe P-A peak acceleration with angle of incidence.

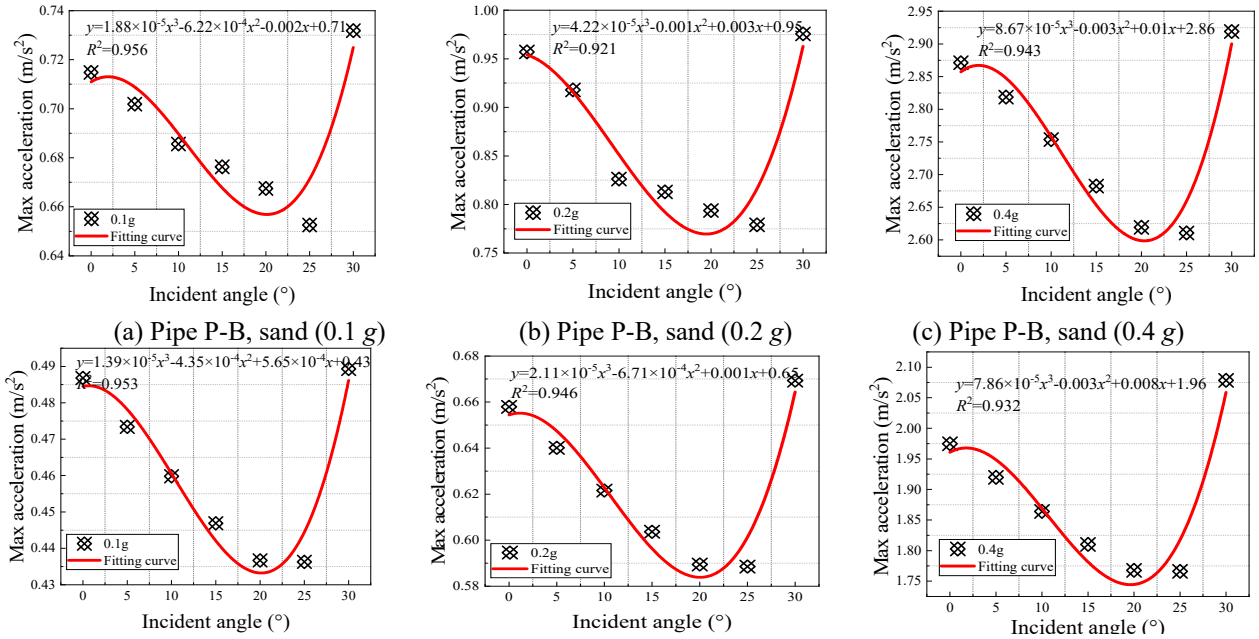

(a) Pipe P-B, sand (0.1 *g*) (b) Pipe P-B, sand (0.2 *g*) (c) Pipe P-B, sand (0.4 *g*)

(d) Pipe P-B, clay (0.1 *g*) (e) Pipe P-B, clay (0.2 *g*) (f) Pipe P-B, clay (0.4 *g*)

Figure 18. Correlation of pipe P-B peak acceleration with angle of incidence.

In summary, there is a strong correlation between the peak acceleration and the angle of incidence for both the utility tunnel and the pipe; therefore, the most unfavorable case of oblique ground shaking incidence should be considered in the seismic design of the utility tunnel system.

7. Conclusion

This paper investigates the dynamic response of a horizontal non-homogeneous field utility tunnel and its internal pipes under the oblique incidence of SV waves, using a viscous-spring artificial boundary and equivalent seismic load. The non-homogeneous field oblique incidence and equivalent seismic load are applied using finite element software and Python. The following conclusions are drawn:

(1) The acceleration response of the utility tunnel and pipe is significantly influenced by the incidence angle. As the incidence angle increases, the horizontal acceleration of the structure first decreases and then increases. At an incidence angle of 30°, the peak acceleration of the utility tunnel and pipe reaches its maximum. Additionally, the depth of the structure influences the acceleration, with deeper structures experiencing lower peak accelerations on the lower side.

(2) The peak ground acceleration (PGA) ranges from 0.1 *g* to 0.4 *g*, with the increment in peak acceleration under the utility tunnel for incidence angles from 0° to 30° showing a difference of approximately 40.7%. This indicates that the incidence angle is more sensitive at higher PGA. The response of different soil types to ground vibration varies, depending on the frequency range of the ground vibrations.

(3) The peak strain in both the utility tunnel and the pipe increases with incidence angle. The magnitude and rate of structural deformation are positively correlated with peak acceleration. The restraining capacity of the angle bearing is superior to that of the concrete pier bearing, while the restraining capacity of the base plate groove is the weakest.

(4) There is a strong correlation between the peak acceleration and the incidence angle for both the utility tunnel and pipe, with correlation coefficients all exceeding 0.8. The utility tunnel provides protective effects for its internal pipe, resulting in a lower rate of change in the pipeline's response compared to that of the utility tunnel. Seismic design for the structure in actual projects should prioritize consideration of the most unfavorable angle of incidence of ground shaking, specifically the angle approaching the critical incidence angle.

(5) Since the input PGA and ground shaking types in this study are insufficient to fully capture the seismic response behavior of the utility tunnel, this aspect will be addressed in future research. Additionally, both vertical and horizontal ground shaking directions will be considered, and the plastic damage of the utility tunnel will be further investigated.

Author contributions

Conceptualization, D.H.; Methodology, S.Y.; Software, H.W.; Validation, D.H.; Formal analysis, Q.L.; Investigation, H.C.; Resources, D.H.; Data curation, C.X.; Writing—original draft preparation, H.W.; Writing—review and editing, D.H., and H.W.; Visualization, Z.H.; Supervision, Z.Z.; Project administration, D.H.; Funding acquisition, D.H. All authors have read and agreed to the published version of the manuscript.

Use of AI tools declaration

The authors declare they have not used Artificial Intelligence (AI) tools in the creation of this article.

Acknowledgments

This research was supported by the National Natural Science Foundation of China(No. 52408537), the Jiangsu Province Key R&D Program (Social Development) Project of China (No. BE2021681), the Natural Science Foundation of Jiangsu Province (No. BK20230693), the China Postdoctoral Science Foundation(No. 2024M752370), the Natural Science Foundation of the Jiangsu Higher Education Institutions of China (No. 23KJB560005), the Key R&D (Social Development) Project of Lianyungang City (No. SF2327), and Lianyungang City Double Creation Doctoral Program, Jiangsu Province Graduate Practice Innovation Program Project (No. SJCX24_2078).

Conflict of Interest

All authors declare no conflicts of interest in this paper.

References

1. Canto-Perello J, Curiel-Esparza J (2013) Assessing governance issues of urban utility tunnels. *Tunnelling Underground Space Technol* 33: 82–87. https://doi.org/10.1016/j.tust.2012.08.007
2. American Public Works Association (1971) Feasibility of utility tunnels in urban areas. APWA Special Report No. 39.

3. Cano-Hurtado JJ, Canto-Perello J (1999) Sustainable development of urban underground space for utilities. *Tunnelling Underground Space Technol* 14: 335–340. https://doi.org/10.1016/S0886-7798(99)00048-6
4. Tang AP, Feng RC, Zhou XY, et al. (2008) Seismic response characteristics of shallow-buried utility tunnel systems. The 14th World Conference on Earthquake Engineering.
5. Jiang L, Chen J, Li J (2010) Seismic response of underground utility tunnels: shaking table testing and FEM analysis. *Earthq Eng Eng Vib* 9: 555–567. https://doi.org/10.1007/s11803-010-0037-x
6. Chen J, Jiang L, Li J, et al. (2012) Numerical simulation of shaking table test on utility tunnel under non-uniform earthquake excitation. *Tunnelling Underground Space Technol* 30: 205–216. https://doi.org/10.1016/j.tust.2012.02.023
7. Sitharam TG, Anitha Kumari SD (2015) Numerical Simulations of Tunnels Using DEM and FEM. Paper presented at the 13th ISRM International Congress of Rock Mechanics, Montreal, Canada.
8. Konstandakopoulou FD, Beskou ND, Hatzigeorgiou GD (2021) Three-dimensional nonlinear response of utility tunnels under single and multiple earthquakes. *Soil Dyn Earthquake Eng* 143: 106607. https://doi.org/10.1016/j.soildyn.2021.106607
9. Yu H, Zhang Z, Chen J, et al. (2018) Analytical solution for longitudinal seismic response of tunnel liners with sharp stiffness transition. *Tunnelling Underground Space Technol* 77: 103–114. https://doi.org/10.1016/j.tust.2018.04.001
10. Zhang J, He C, Geng P, et al. (2019) Improved longitudinal seismic deformation method of shield tunnels based on the iteration of the nonlinear stiffness of ring joints. *Sustainable Cities Soc* 45: 105–116. https://doi.org/10.1016/j.scs.2018.11.019
11. Zhang W, Restrepo D, Crempien JG, et al. (2021) A computational workflow for rupture-to-structural-response simulation and its application to Istanbul. *Earthquake Eng Struct Dyn* 50: 177–196. https://doi.org/10.1002/eqe.3377
12. Zhang W, Taciroglu E (2021) 3D time-domain nonlinear analysis of soil-structure systems subjected to obliquely incident SV waves in layered soil media. *Earthquake Eng Struct Dyn* 50: 2156–2173. https://doi.org/10.1002/eqe.3443
13. Panji M (2023) A half-space TD-BEM model for a seismic corrugated orthotropic stratum. *Eng Anal Boundary Elem* 152: 655–677. https://doi.org/10.1016/j.enganabound.2023.04.032
14. Kavandi P, Ganjian N, Panji M (2024) A DR-BEM approach for analyzing the transient SH-wave scattering problems: A comparative study. *Eng Anal Boundary Elem* 169: 105962. https://doi.org/10.1016/j.enganabound.2024.105962
15. Mojtabazadeh-Hasanlouei S, Panji M, Kamalian M (2022) Scattering attenuation of transient SH-wave by an orthotropic gaussian-shaped sedimentary basin. *Eng Anal Boundary Elem* 140: 186–219. https://doi.org/10.1016/j.enganabound.2022.04.023
16. Mojtabazadeh-Hasanlouei S, Panji M, Kamalian M (2022) Attenuated orthotropic time-domain half-space BEM for SH-wave scattering problems. *Geophys J Int* 229: 1881–1913. https://doi.org/10.1093/gji/ggac032
17. Li M, Zhang K, Meng K, et al. (2023) Seismic response study of shield tunnel with lateral karst cavity under SV waves. *Structures* 56: 105023. https://doi.org/10.1016/j.istruc.2023.105023
18. Li M, Meng K, Zhou J, et al. (2024) Seismic response and damage analysis of shield tunnel with bottom Karst caves under oblique SV waves. *Nat Hazards* 120: 2731–2747. https://doi.org/10.1007/s11069-023-06302-5

19. Zarzalejos JM, Aznárez JJ, Padrón LA, et al. (2014) Influences of type of wave and angle of incidence on seismic bending moments in pile foundations. *Earthquake Eng Struct Dyn* 43: 41–59. https://doi.org/10.1002/eqe.2330
20. Huang JQ, Du XL, Zhao M, et al. (2017) Impact of incident angles of earthquake shear (S) waves on 3-D non-linear seismic responses of long lined tunnels. *Eng Geol* 222: 168–185. https://doi.org/10.1016/j.enggeo.2017.03.017
21. Ye Z, Li Y, Li L, et al. (2025) Seismic response of a long shield tunnel crossing through multiple soil deposits. *Comput Geotech* 177: 106892. https://doi.org/10.1016/j.compgeo.2024.106892
22. Yan L, Haider A, Li P, et al. (2020) A numerical study on the transverse seismic response of lined circular tunnels under obliquely incident asynchronous P and SV waves. *Tunnelling Underground Space Technol* 97: 103235. https://doi.org/10.1016/j.tust.2019.103235
23. Du XL, Li LY (2008) A Viscoelastic Artificial Boundary for Near-field Fluctuation Analysis of Saturated Porous Media. *Chin J Geophys* 51: 575–581.
24. Qu J (2017) Dynamic response of comprehensive pipe gallery under oblique incident seismic wave. Harbin Institute of Technology.
25. Zhao J, Lan WJ, Teng WQ, et al. (2021) Three-dimensional seismic response analysis of submarine immersed tube tunnel considering oblique incidence of P wave. *Struct Eng* 37: 73–81.
26. Wang Z, Jing LP, Lu XY, et al. (2023) Comparative Study on Viscoelastic Artificial Boundary Elements and round Motion Input Methods. *World Earthquake Eng* 39(2).
27. Wang F, Song Z, Liu Y, et al. (2023) Response Characteristics and Tensile Failure Evaluation of Asphalt Concrete Core Wall under Oblique Incidence of SV Wave Space. *Chin J Geotech Eng* 45: 1733–1742.
28. Du XL, Xu HB, Zhao M (2015) Analysis of seismic response of high arch dam under SV wave oblique incidence. *J Hydropower Gener* 34: 139–145
29. Huang ZY, Feng YZ, Tang AP, et al. (2023) Influence of oblique incidence of P-waves on seismic response of prefabricated utility tunnels considering joints. *Soil Dyn Earthquake Eng* 167: 107797. https://doi.org/10.1016/j.soildyn.2023.107797
30. Yu J, Wang ZZ (2021) The dynamic interaction of the soil-tunnel-building system under seismic waves. *Soil Dyn Earthquake Eng* 144: 106686. https://doi.org/10.1016/j.soildyn.2021.106686
31. Zhou Tl, Dong CS, Li S, et al. (2024) Seismic response of tunnel with damping layer under oblique incident SV wave. *World Earthquake Eng* 40: 1–12.
32. Lysmer J, Kuhlemeyer RL (1969) Finite dynamic model for infinite media. *J Eng Mech Div* 95: 859–877. https://doi.org/10.1061/JMCEA3.0001144
33. Xu CS, Hu ZY, Shi YB, et al. (2022) Seismic response law of prefabricated integrated utility tunnel interface under oblique incidence of SV wave. *J Beijing Univ Technol* 48: 1215–1225.
34. Wang GB, Yuan MZ, Miao Y, et al. (2018) Experimental study on seismic response of underground tunnel-soil-surface structure interaction system. *Tunnelling Underground Space Technol* 76: 145–159. https://doi.org/10.1016/j.tust.2018.03.015

AIMS Press

© 2025 the Author(s), licensee AIMS Press. This is an open access article distributed under the terms of the Creative Commons Attribution License (http://creativecommons.org/licenses/by/4.0)